

Analysis of matter clustering in one dimension with the Gaussian-derived wavelet

YUN WANG ¹, HUA-YU YANG ¹ AND PING HE ^{1,2}

¹College of Physics, Jilin University, Changchun 130012, P.R. China.

²Center for High Energy Physics, Peking University, Beijing 100871, P.R. China.

ABSTRACT

Continuous wavelet analysis has been increasingly employed in various fields of science and engineering due to its remarkable ability to maintain optimal resolution in both space and scale. Here, we extend wavelet-based statistics, including the wavelet power spectrum, wavelet cross-correlation and wavelet bicoherence, to the new designed continuous wavelet function – *Gaussian-derived wavelet*. In this paper, these statistics are introduced to analyze the large-scale clustering of matter. For this purpose, we perform wavelet transforms on the density distribution obtained from the one-dimensional (1D) Zel’dovich approximation and then measure the wavelet power spectra and wavelet bicoherences of this density distribution. Our results suggest that the wavelet power spectrum and wavelet bicoherence can identify the effects of local environments on the clustering at different scales. Moreover, to reveal the usefulness of the wavelet cross-correlation, we apply it to the 1D projected density fields of the IllustrisTNG simulation at $z = 0$ for different matter components. We find that wavelet cross-correlations between different matter components converge to one on large scales, while biases between them become significant on small scales. In addition, measurements of the wavelet power spectra show that clustering of the total matter is suppressed on scales $k \gtrsim 1 \text{ hMpc}^{-1}$ relative to that of the corresponding dark matter-only simulation. The wavelet bicoherence of the total matter is enhanced on wide scales due to baryonic physics. These results are qualitatively consistent with those from three-dimensional Fourier analyses.

Unified Astronomy Thesaurus concepts: [Wavelet analysis \(1918\)](#); [Dark matter \(353\)](#); [Intergalactic medium \(813\)](#); [Large-scale structure of the universe \(902\)](#)

1. INTRODUCTION

The standard cosmological model (Λ CDM) states that the hierarchical matter clustering evolved from the random primordial fluctuations via gravitational instability, as revealed by the observed pattern of spatial distribution for luminous objects (Tegmark et al. 2004). However, luminous objects are made up of baryons, whose clustering is not completely consistent with that of dark matter (DM) component because of a series of physical processes such as radiative cooling, star formation and feedback processes. With hybrid N -body/hydrodynamic simulations, the baryonic effects on the large-scale clustering of matter have been extensively studied in Fourier space, and these studies show that the deviation between baryons and dark matter in mass distribution depends on the scale and redshift (Chisari et al. 2019; van Daalen et al. 2020; Yang et al. 2020). Moreover, many studies indi-

cate that the clustering of both dark matter and baryonic matter is environment-dependent (Abbas & Sheth 2005; Peng et al. 2010; Wang et al. 2018; Man et al. 2019). However, usual statistical schemes based on the Fourier transform, e.g. power spectrum and bispectrum, cannot be used to measure the environmental and scale dependence of the matter clustering at the same time, since these schemes cannot simultaneously provide information about the scale and position of the signal. One way to overcome this problem is to use techniques of the wavelet transform, which is a powerful tool for analysing space-scale information simultaneously.

Wavelet transform analysis decomposes a signal into separate scale components using a set of scaled and shifted wavelets, which are well localized in both real and Fourier space. Consequently, the local features of the signal at different scales are revealed by this decomposition. Wavelet transform methods can be classified into the discrete wavelet transform (DWT) and the continuous wavelet transform (CWT). The DWT, using orthogonal wavelet bases, operates over scales and positions based on the integer power of two, hence giving the most compact representation of the signal.

This leads to the effectiveness and ease of implementation of the DWT, which hence is particularly useful for information compression (Khalifa et al. 2008; Abdulazeez et al. 2020). Due to its advantages, the DWT has also been applied to study the large-scale structure of the universe (Pando & Fang 1996; Pando et al. 1998; Fang & Feng 2000; Liu & Fang 2008). However, there are mainly two drawbacks in the DWT caused by dyadic scales. Firstly, the DWT provides the poor scale resolution so that some meaningful features of a signal cannot be detected. Secondly, it lacks translational invariance. The so-called translational invariance means that if a signal is translated, then its wavelet coefficients is translated by the same amount without other modification at every scales (Addison 2017). Obviously it is not the case for the DWT. A small translation on the signal can make the discrete wavelet coefficients vary substantially on different scales, thereby the total energy in the wavelet domain being not conserved after the signal was shifted. These drawbacks suggest that the DWT is not suitable for analyzing signals with extremely high complexity.

In contrast to the DWT, the CWT allows the scale and translation parameters to continuously change, which makes it translational invariant and redundant. The redundancy guarantees that the CWT can provide high resolution results, which are much easier to interpret than those obtained with the DWT (Aguiar-Conraria & Soares 2014; Addison 2018). As a result, the CWT is becoming more and more popular across different disciplines, including geophysics, biomedicine, economics, astrophysics, fluid mechanics and so on (Addison 2018). For instance in astrophysics and cosmology, the CWT is used for the detection of 21cm signal (Gu et al. 2013), the detection of baryonic acoustic oscillations (Tian et al. 2011; Arnalte-Mur et al. 2012; Labatie et al. 2012), the detection of substructures in 2D mass maps (Flin & Krywult 2006; Schwinn et al. 2018), the analysis of turbulence evolution in the intracluster medium (Shi et al. 2018), the correlation analysis of galactic images (Frick et al. 2001; Tabatabaei et al. 2013) and the analysis of the multifractal character of the galaxy distribution (Martínez et al. 1993; Rozgacheva et al. 2012).

The main problem faced by the CWT, e.g. when analyzing one-dimensional (1D) signals, is that its classical inverse formula is a double integration, which results in a heavy computational effort for recovering the original signal. Although there is an alternative inverse transform formula in the form of single-integral for the complex-valued wavelets, the real wavelets has generally been considered to have no such simple inverse transformation (Delprat et al. 1992; Aguilar-Conraria & Soares 2014). In our previous work (Wang & He 2021), we proposed a novel scheme of constructing continuous wavelets to overcome this problem, in which the wavelet functions are obtained by taking the first derivative

of smoothing functions with regard to the positive defined scale parameter. With this scheme, the original signal is recovered easily by integrating the wavelet coefficients with respect to the scale parameter. As an inspired example, we took the Gaussian function as a smoothing function to derive the wavelet dubbed the *Gaussian-derived wavelet* (hereafter GDW) and briefly discussed its preliminary application to the matter power spectrum, demonstrating the success of this scheme.

In this work, we use local statistics established on wavelet coefficients to further investigate the potential of GDW for analyzing the large-scale clustering of matter. Specifically, the wavelet power spectrum (WPS), the wavelet cross-correlation (WCC), and the wavelet bicoherence (WBC) are employed here. The WPS and WCC were first introduced by Hudgins et al. (1993) to examine atmospheric turbulence. The WPS measures the variance of a signal at various scales within some local region, and the WCC is used to quantify similarities between two signals. The WBC was originally proposed by van Milligen et al. (1995a,b) to detect the short-lived structures induced by phase coupling in turbulence. Moreover, the cosmic baryonic density distribution at late times is similar to a fully developed turbulence (Shandarin & Zeldovich 1989; He et al. 2006), which enlightens us to apply these tools to the context of structure formation of the universe. To illustrate our approach in a more intuitive way, we shall use the one-dimensional (1D) matter distributions, since a great deal of work on the large-scale structure of the universe is accomplished using 1D cosmology models (Gouda & Nakamura 1989; Fujiwara & Soda 1996; Tatekawa & Maeda 2001; Miller & Rouet 2010; Manfredi et al. 2016). The Zel'dovich approximation is a simple model that provides a good approximated solution for the nonlinear evolution of collisionless matter (Zel'dovich 1970). In the 1D case, the Zel'dovich approximation is proved to be an exact solution in the fully nonlinear regime until the first singularity appears (Soda & Suto 1992). It is straightforward and efficient to calculate the 1D Zel'dovich solution, and so we discuss our analysis method with it. Firstly, we decompose the density fields obtained from the 1D Zel'dovich approximation into wavelet components at different positions and scales. Then, by measuring the WPS and WBC of matter densities based on these components, we investigate the effects of density environment on the matter clustering. To demonstrate the role of the WCC in the analysis of clustering, we apply it to the 1D projected density fields for different matter components in the IllustrisTNG simulation (Springel et al. 2018; Naiman et al. 2018; Nelson et al. 2018; Pillepich et al. 2018; Marinacci et al. 2018). It is expected that the WCC can give approximately correct bias between different matter distributions. As a supplement, we also examine the baryonic effects on the WPS and WBC of total matter.

Table 1. Notations used in the paper, with their meanings and Acronyms

Notation	Meaning	Acronym
$\psi(w, x)$	Gaussian-derived wavelet	GDW
$\hat{\psi}(w, k)$	Fourier transform of the GDW	
$W_f(w, x)$	wavelet transform	WT
$\hat{W}_f(w, k)$	Fourier transform of the WT	
$P_f^{W,L}(w)$	wavelet power spectrum	WPS
$P_f(k)$	Fourier power spectrum	
$XWT_{fg}(w, x)$	cross-wavelet transform	XWT
$C_{fg}^{W,L}(w)$	wavelet cross-correlation	WCC
$E_f^{W,L}(w_1, w_2)$	wavelet bispectrum	WBS
$b_f^{W,L}(w_1, w_2)$	wavelet bicoherence	WBC
$b_f^{W,L}(w)$	summed WBC	
$b_f^{W,L}$	total WBC	

This paper is organized as follows. In section 2, we describe the characteristic of the GDW, the theory of the CWT and wavelet-based statistical tools. In section 3, we briefly introduce the data we used, including one-dimensional Zel'dovich approximation and density fields in IllustrisTNG. In section 4, we give the numerical results for the matter clustering. Finally in section 5, we discuss and summarize our results.

2. METHODS OF CONTINUOUS WAVELET ANALYSIS

In this section, we briefly review the definition of the CWT based on the GDW and then introduce the wavelet-based statistical tools, i.e. the WPS, the WCC function and the WBC. To assess their significance, statistical errors are then discussed. Finally, we give the correspondence between the wavelet scale and the Fourier wavenumber for the GDW.

2.1. The Gaussian-derived wavelet and the continuous wavelet transform

The GDW, used in this work, is defined as the first derivative of the Gaussian smoothing function with respect to the scale parameter,

$$\begin{aligned} \psi(w, x) &\equiv \sqrt{w} \frac{\partial G(w, x)}{\partial w} \\ &= \frac{\sqrt{w}}{4\sqrt{\pi}} (2 - w^2 x^2) \exp\left(-\frac{w^2 x^2}{4}\right), \end{aligned} \quad (1)$$

where $G(w, x) = w \exp(-w^2 x^2/4) / (2\sqrt{\pi})$ denotes the Gaussian smoothing function with the scale parameter w greater than zero. The prefactor \sqrt{w} on the right hand side of equation (1) ensures that the energy of the wavelet is unaffected by the scale parameter¹. The Fourier transform of the GDW is given by

$$\hat{\psi}(w, k) = \frac{2}{\sqrt{w}} \left(\frac{k}{w}\right)^2 \exp\left[-\left(\frac{k}{w}\right)^2\right], \quad (2)$$

through which the scale parameter w is defined as the peak wavenumber of $\hat{\psi}(w, k)$, i.e. the wavenumber at which $\hat{\psi}(w, k)$ takes the maximum value, as demonstrated in Fig. 1. It can be seen from equation (1) and (2) that the GDW satisfies the conditions of admissibility, similarity and regularity. In fact, the GDW is the same as the Mexican hat wavelet in one dimension, except for their constant factors. This is illustrated by substituting $w = \sqrt{2}/a$ into equation (1), where a is the scale parameter for the traditional CWT. However, as pointed out by Wang & He (2021), the 3D GDW is an anisotropic separable wavelet function, which is not a 3D Mexican hat wavelet. At present, we concern only the 1D case.

The wavelet function $\psi(w, x)$ is then used to perform the wavelet transform of a one-dimensional signal $f(x)$ as follows

$$W_f(w, x) = \int_{-\infty}^{+\infty} f(u) \psi(w, x - u) du, \quad (3)$$

Note that there is no complex conjugate in equation (3) since both signal and wavelet are real. The wavelet transform, equation (3), is nothing but a convolution of the signal with wavelets at different scales, which can be implemented efficiently by FFT technique. As a function of scale w and space x , from the wavelet transform we can clearly see the different scale features which are well localized in space. However, it is not possible to achieve arbitrarily good resolution in space and scale simultaneously (Chui 1997; Addison 2017). As illustrated in Fig. 1, a narrower (wider) wavelet provides better (poorer) spatial resolution accompanied by poorer (better) frequency resolution. This fact is quantified in terms of the uncertainty principle $\delta x \delta k \gtrsim 1/2$ for the GDW, where δx is the standard deviation of the wavelet in real space and δk is the standard deviation in frequency (Chui 1997).

The greatest convenience brought to us by the definition of GDW is that the signal can be reconstructed through a single integral of the wavelet coefficients. Combining equation (1) and (3), we have

$$W_f(w, x) = \sqrt{w} \frac{\partial f_s(w, x)}{\partial w}, \quad (4)$$

¹ In the first paper (Wang & He 2021), we simply define GDW as $\psi(w, x) \equiv \partial G(w, x) / \partial w$.

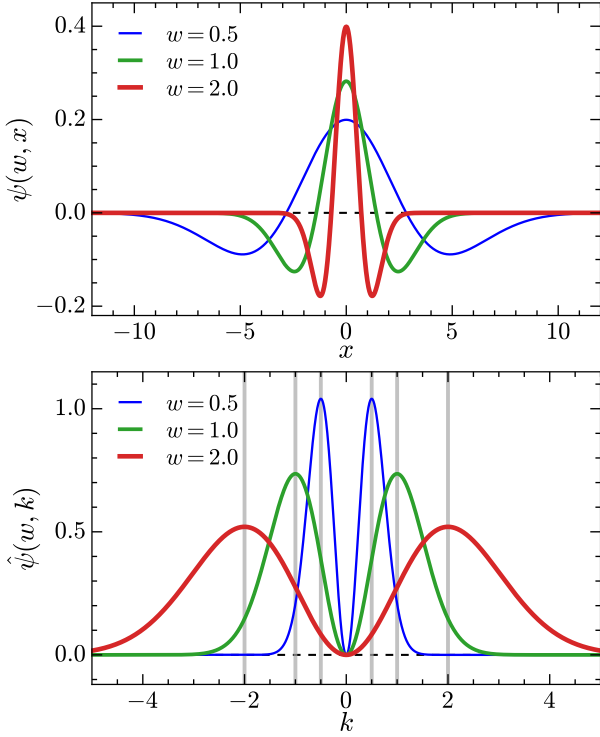


Figure 1. The Gaussian-derived wavelet, $\psi(w, x) = \sqrt{w}(2 - w^2x^2) \exp(-w^2x^2/4)/(4\sqrt{\pi})$ (top) and the corresponding Fourier transform $\hat{\psi}(w, k)$ (bottom) for three scale parameters, $w = 0.5, 1.0$ and 2.0 . The grey vertical lines denote wavenumbers where $\hat{\psi}(w, k)$ takes the maximum.

where $f_s(w, x)$ refers to the smoothed field and is given by

$$f_s(w, x) = \int_{-\infty}^{+\infty} f(u)G(w, x - u)du. \quad (5)$$

By integrating equation (4) with respect to w , we get the single integral inverse transform as shown below,

$$f(x) = C + \int_0^{+\infty} \frac{W_f(w, x)}{\sqrt{w}} dw, \quad (6)$$

where the integral constant C is equal to $\lim_{w \rightarrow 0} f_s(w, x)$. Compared with the usual reconstruction formula for the CWT found in most wavelet literatures, e.g. Addison (2017), our reconstruction formula defined by equation (6) is much easier to compute numerically and generalize to integrations of higher dimensions.

2.2. Parseval's theorem for the continuous wavelet transform

Parseval's theorem is an important result in Fourier Transform, which states that the inner product between signals is preserved in going from time to the frequency domain. Similarly, there is an analogue of Parseval's theorem for the wavelet transform (Hudgins et al. 1993), the form of which

is expressed as

$$\begin{aligned} & \int_0^{+\infty} \int_{-\infty}^{+\infty} W_f(w, x)W_g(w, x)dx dw \\ &= C_\psi \int_{-\infty}^{+\infty} f(u)g(u)du, \end{aligned} \quad (7)$$

where $C_\psi = \int_0^{+\infty} (\hat{\psi}(1, k)^2/k)dk$ is the admissibility constant, and it equals to $1/2$ for the GDW. If f and g are the same, then we have

$$\int_0^{+\infty} \int_{-\infty}^{+\infty} |W_f(w, x)|^2 dx dw = C_\psi \int_{-\infty}^{+\infty} |f(u)|^2 du. \quad (8)$$

2.3. The wavelet power spectrum and the wavelet cross-correlation

We assume that the signal $f(x)$ satisfies the periodic boundary condition with period L_b , which is a usual choice for studying a typical region of the universe. Then for a sub-region of the signal $L \leq L_b$, the local WPS is defined as

$$P_f^{W,L}(w) = \frac{1}{L} \int_L |W_f(w, x)|^2 dx. \quad (9)$$

We can see that equation (9) refers to the variance at the scale w within the spatial region L , since $|W_f(w, x)|^2$ just the variance per area at the space-scale plane, as referred to by the Parseval's theorem, equation (8). According to the Fourier Parseval's theorem for periodical signals, we can obtain the relationship between the global wavelet and Fourier power spectrum, which is given by

$$\begin{aligned} P_f^{W,L_b}(w) &= \frac{1}{L_b} \int_0^{L_b} |W_f(w, x)|^2 dx \\ &= \frac{1}{L_b} \sum_k \frac{|\hat{W}_f(w, k)|^2}{L_b} \\ &= \sum_k P_\psi(w, k)P_f(k), \end{aligned} \quad (10)$$

where $\hat{W}_f(w, k) = \hat{\psi}(w, k)\hat{f}(k)$ is the Fourier transform of $W_f(w, x)$, $P_f(k) = |\hat{f}(k)|^2/L_b$ is the Fourier power spectrum of the signal, and $P_\psi(w, k) = |\hat{\psi}(w, k)|^2/L_b$ denotes the Fourier power spectrum of the wavelet. Obviously, the global WPS of a signal is the average of its Fourier power spectrum weighted by the Fourier power spectrum of the corresponding wavelet function over all wavenumbers.

Then given two signals $f(x)$ and $g(x)$ with wavelet transforms $W_f(w, x)$ and $W_g(w, x)$, we can define the XWT as

$$XWT_{fg}(w, x) = W_f(w, x)W_g(w, x), \quad (11)$$

i.e. it measures the local covariance at each spatial position and scale, as revealed by equation (7). By integrating the XWT over a finite spatial region, we get the normalized local WCC as follows

$$C_{fg}^{W,L}(w) = \frac{1}{L} \frac{\int_L XWT_{fg}(w, x) dx}{(P_f^{W,L} P_g^{W,L})^{1/2}}, \quad (12)$$

which can take on values between -1 (perfect anti-correlation) and 1 (perfect correlation).

2.4. The wavelet bicoherence and error estimation

The main content of this sub-section is based on [van Milligen et al. \(1995a,b\)](#), and we refer the interested readers to these two references for detail.

The Fourier bispectrum is the lowest order statistic that measures the amount of phase-coupling of harmonic modes within a signal. By analogy to it, the WBS is given as

$$B_f^{W,L}(w_1, w_2) = \frac{1}{L} \int_L W_f(w_1, x) W_f(w_2, x) W_f(w, x) dx, \quad (13)$$

where $w_1 + w_2 = w$ (frequency sum rule). The WBS measures the non-linear interplay within the local region L between scale components w_1 , w_2 and w such that the sum rule is satisfied. In the case of completely random phases of the signal, $B_f^{W,L}(w_1, w_2)$ is statistically to be zero. However, once a coherent structure is formed by the phase-coupling, $B_f^{W,L}(w_1, w_2)$ will take significant non-zero values. The WBS usually is normalized in the following way:

$$b_f^{W,L}(w_1, w_2) = \left[\frac{|B_f^{W,L}(w_1, w_2)|^2}{\frac{1}{L} \int_L |W_f(w_1, x) W_f(w_2, x)|^2 dx P_f^{W,L}} \right]^{1/2}, \quad (14)$$

which is called the WBC, attaining values between 0 and 1. Throughout this paper, we will use it to measure the non-linear behaviors of matter clustering instead of the WBS. In addition, it is convenient to introduce the summed WBC defined as

$$b_f^{W,L}(w) = \left[\frac{1}{s(w)} \sum_{w_1, w_2} [b_f^{W,L}(w_1, w_2)]^2 \right]^{1/2}, \quad (15)$$

where the summation is taken over all w_1 and w_2 such that $w_1 + w_2$ equals to w and $s(w)$ is the number of summands in the summation. In addition, as a measure of the total non-linearity in the chosen region of the signal, the total WBC is defined by averaging the squared WBC over all points in the scale-scale plane as

$$b_f^{W,L} = \left[\frac{1}{S} \sum_{w_1, w_2} [b_f^{W,L}(w_1, w_2)]^2 \right]^{1/2}, \quad (16)$$

where S is the total number of points (w_1, w_2) in the scale-scale plane.

In practice for discrete sampled signals, integrations over the interval L involved in calculating the statistics mentioned above are carried out with summation over N sample points. By the law of large numbers, an integration over L suffers a relative statistical error of $1/\sqrt{N}$. In addition, the fact that CWTs are non-orthogonal leads to that wavelet coefficients are not all statistically independent ([van Milligen et al. 1995a,b, 1997](#)). If continuous wavelets $\psi(x)$ and $\psi^*(x + d_0)$ satisfy $\int \psi(x)\psi^*(x + d_0)dx = 0$, then they can be regarded as approximately orthogonal and corresponding wavelet coefficients are statistically independent. In the case of GDW, independent wavelet coefficients are separated by distance d_0/w at each scale, where $d_0 = 2\sqrt{3} - \sqrt{6}$. Then the number of statistical independent points on the interval L is $N' = L/(d_0/w) = 2\pi Nw/(d_0 k_{\text{samp}})$, where $k_{\text{samp}} = 2\pi/\Delta x$ is the sampling frequency. Thus for the WPS, its statistical error is estimated by

$$\epsilon [P_f^{W,L}(w)] \approx \frac{P_f^{W,L}(w)}{\sqrt{N'}} = P_f^{W,L}(w) \left(\frac{d_0 k_{\text{samp}}}{2\pi Nw} \right)^{1/2}. \quad (17)$$

By applying similar estimates for all integral terms in equation (12) and according to error propagation, we obtain the statistical noise level for the WCC,

$$\epsilon [C_{fg}^{W,L}(w)] \approx \left(\frac{3d_0 k_{\text{samp}}}{4\pi Nw} \right)^{1/2}. \quad (18)$$

Equation (18) is called the statistical noise level, because it is the cross-correlation value that can be achieved by a Gaussian noise and is caused by using a limited number of values in the integration. Notice that this noise level is scale-dependent, suggesting that the interpretation of the signal becomes increasingly significant as the scale decreases. Just like the approach above, we can obtain the noise level of the WBC shown below,

$$\epsilon [b_f^{W,L}(w_1, w_2)] \approx \left(\frac{d_0 k_{\text{samp}}}{2\pi N \text{Min}(w_1, w_2, w_1 + w_2)} \right)^{1/2}. \quad (19)$$

2.5. The relationship between scale and wavenumber

To facilitate the comparison between wavelet and Fourier spectra, we need to ascertain the relationship between the scale parameter w and the equivalent Fourier wavenumber. [Meyers et al. \(1993\)](#) and [Torrence & Compo \(1998\)](#) suggest that the relationship between them can be derived analytically for a particular wavelet function by performing wavelet transform of a cosine wave with known period, such as $\cos(k_F x)$, and then computing the scale w at which the scalogram reaches its maximum. Following their method,

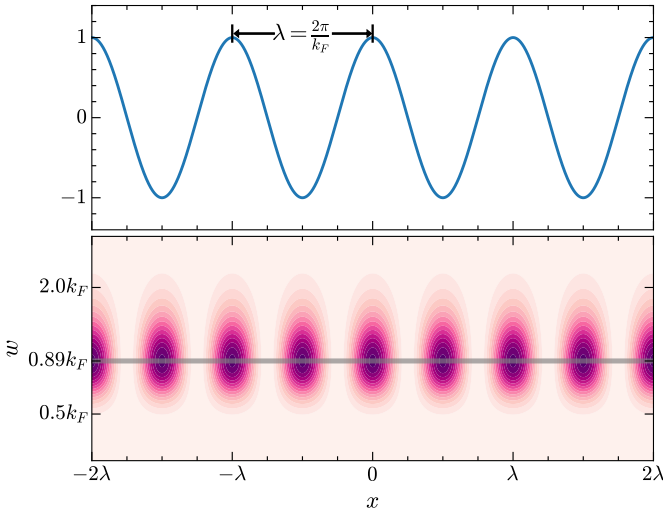


Figure 2. The squared wavelet transform plot of a cosine function. Upper panel: a cosine wave of period $\lambda = 2\pi/k_F$. Lower panel: the corresponding contour plot of $|W_{\cos}(w, x)|^2$ for the cosine wave. The gray horizontal line indicates that $|W_{\cos}(w, x)|^2$ takes its maximum value at $w \approx 0.89k_F$.

the scalogram of $\cos(k_F x)$ is first computed with the GDW, and the result is

$$|W_{\cos}(w, x)|^2 = \frac{4k_F^4 \cos^2(k_F x) \exp(-\frac{2k_F^2}{w^2})}{w^5}, \quad (20)$$

which is depicted in Fig. 2. The scale parameter that makes $|W_{\cos}(w, x)|^2$ take the maximum value should be equivalent to the wavenumber k_F , since the Fourier power spectrum of a cosine wave is an impulse at k_F . Therefore, by solving $\partial|W_{\cos}(w, x)|^2/\partial w = 0$, we get the correspondence between the wavelet scale and Fourier wavenumber,

$$w = \frac{2}{\sqrt{5}}k_F \approx 0.89k_F. \quad (21)$$

The relation of equation (21) shows that the wavelet scale is proportional to the Fourier wavenumber. In the next sections, we will present our results in terms of the equivalent Fourier wavenumber k_F instead of w , and we drop the subscript ‘ F ’ for simplicity of notation.

For convenience of readers, in Table 1, we list all the notations used in our paper, with their meanings and the corresponding acronyms.

3. DATA SETS

In this work, we use two types of data, i.e. the 1D density fields obtained from Zel’dovich approximation and IllustrisTNG simulations, respectively. In the 1D case, Zel’dovich approximation provides the exact non-linear solution for the perturbative equations of collisionless matter up to the first appearance of orbit-crossing singularities (Soda & Suto 1992). Due to easy implementation and fast computation of

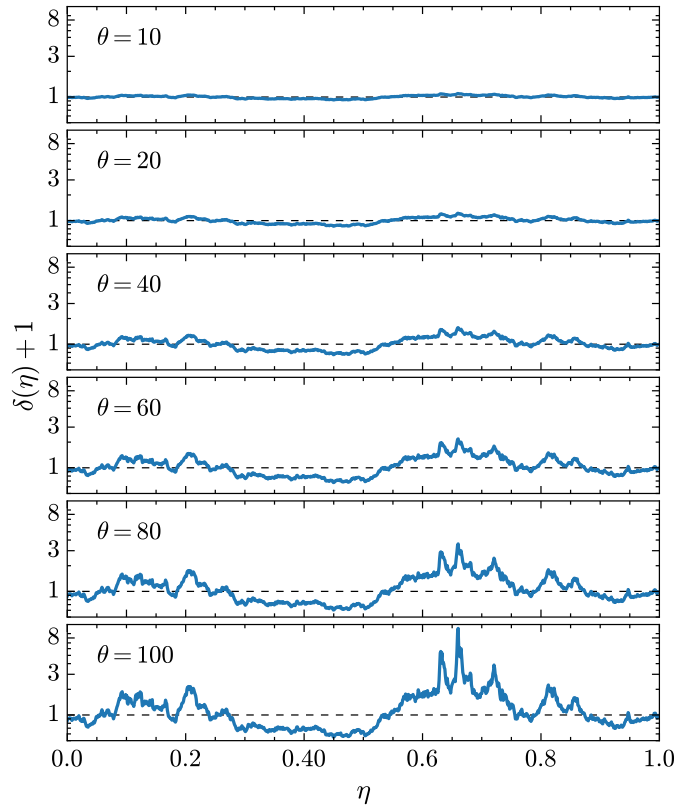


Figure 3. The one-dimensional density fields obtained from Zel’dovich approximation at times $\theta = 10, 20, 40, 60, 80$ and 100 from top to bottom.

the 1D Zel’dovich exact solution, we will demonstrate the usefulness of our method with it. However, Zel’dovich approximation is only for collisionless matter, i.e. dark matter. For measuring the cross-correlation of different matter by the WCC, we also consider the 1D projected density fields of IllustrisTNG simulation.

3.1. Zel’dovich approximation in one dimension

The fundamental idea of Zel’dovich approximation is the transformation between Eulerian and Lagrangian coordinates, i.e.

$$x(t, q) = q - \theta(t)f(q), \quad (22)$$

where x and q are the Eulerian and Lagrangian coordinate, respectively. Then by applying the mass conservation to equation (22), the density contrast is given explicitly by

$$\delta(\eta, t) + 1 = \frac{1}{1 - \theta(t)F(\eta)}, \quad (23)$$

where $F(\eta) = \frac{df(\eta L_b)}{d\eta}/L_b$ with $\eta = q/L_b$ being the dimensionless coordinate divided by the length size of density field, and $\theta(t)$ is the growth factor. For simplicity, we normalize $\theta(t)$ to unity at the initial time and use it as a time

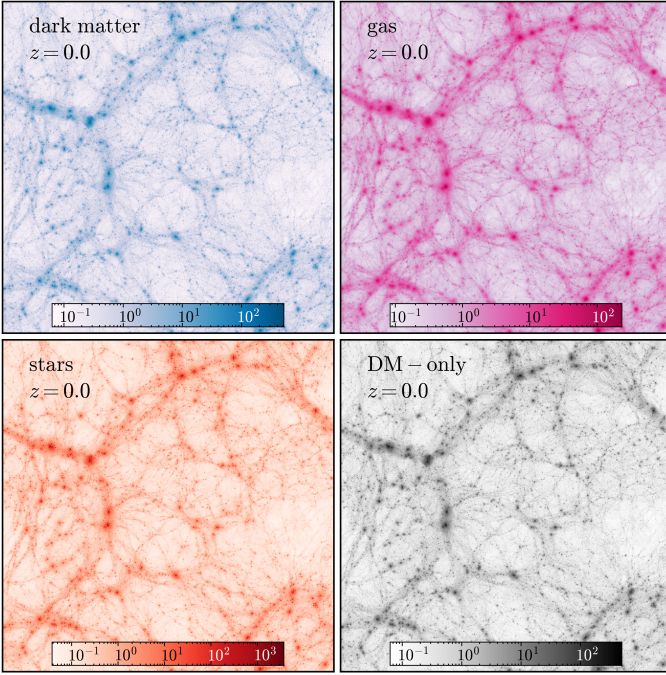


Figure 4. The two-dimensional projected density fields of dark matter (top left), gas (top right), stars (bottom left) in TNG100 and the two-dimensional density field in the corresponding DM-only simulation (bottom right) at redshift $z = 0$. The slices are $75 \times 75 h^{-2} \text{Mpc}^2$, with a thickness $25 h^{-1} \text{Mpc}$.

variable instead of t . It is easy to see from equation (23) that $F(\eta)$ is the initial density contrast if small enough. For more details about the one-dimensional Zel’dovich approximation, we refer the readers to Soda & Suto (1992) and Fujiwara & Soda (1996).

The initial condition is set to be

$$F(\eta) = 2 \sum_{k>0} \sqrt{P_1(k)} [B_k \cos(k\eta) + C_k \sin(k\eta)], \quad (24)$$

where B_k and C_k are drawn from Gaussian with standard deviation of 1. We impose periodic boundary condition on the interval $\eta \in [0, 1]$, then divide it into 1024 equally spaced segments. So the wave number, as an integer multiple of 2π , has a maximum value of $512 \cdot 2\pi$, i.e. the Nyquist frequency. In this work, we assume that the spectral index of the initial power spectrum $P_1(k) = Ak^n$ in equation (24) is equal to $n = -2$. The amplitude A is chosen to be 2.5×10^{-6} such that the initial density perturbation is between -0.01 and 0.01 . Hence evolution of the density field is totally determined by equation (23) and (24).

As shown in Fig. 3, we select the density fields at $\theta = 10, 20, 40, 60, 80,$ and 100 to examine their evolution from linear to non-linear stages.

3.2. IllustrisTNG data

The IllustrisTNG project is a suite of state-of-the-art cosmological hydrodynamic simulations (Springel et al. 2018;

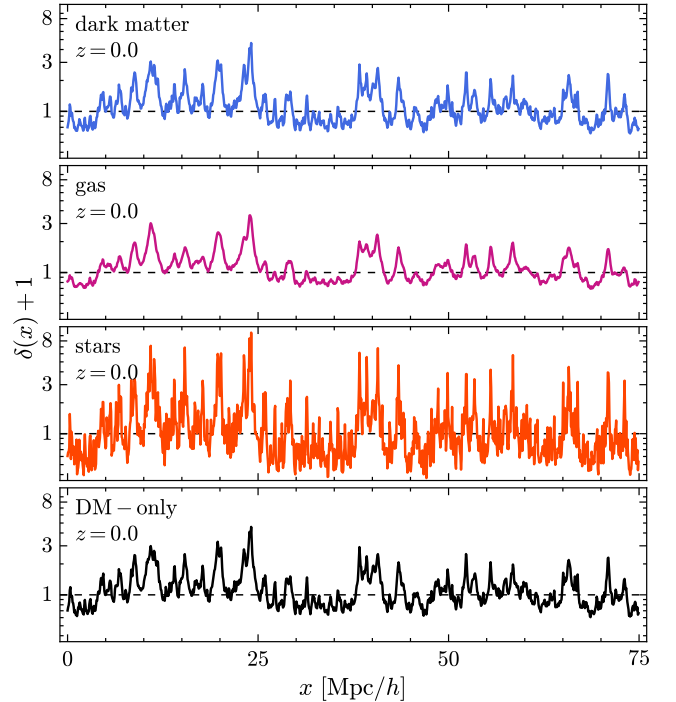


Figure 5. One-dimensional density fields of different matter components obtained by projecting the two-dimensional ones shown in Fig. 4 onto the horizontal axis.

Naiman et al. 2018; Nelson et al. 2018; Pillepich et al. 2018; Marinacci et al. 2018), which were executed with the moving-mesh code AREPO (Springel 2010). With a comprehensive galaxy formation model built into AREPO, IllustrisTNG (hereafter TNG) is capable of realistically tracking the clustering evolution of dark matter and baryons in the universe. The TNG suite includes three simulation volumes: TNG100, TNG300 and TNG50. In this study, we focus on the TNG100 simulation whose box size is $75 h^{-1} \text{Mpc}$. We use cloud-in-cell (CIC) assignment scheme to assign all the mass points to a 1024^3 uniform mesh, thereby obtaining mass density distribution at Cartesian grids. Fig. 4 shows the two-dimensional projections of matter density fields, including dark matter, gas, stars and the corresponding DM-only run, at redshifts $z = 0$. Similar to what Springel et al. (2018) did in measuring the cross-correlation functions between different matter, we here put the black holes and stars together, and then labeled as stars. In order to apply the 1D CWT, we further project the density fields of these two-dimensional slices onto the horizontal axis, by which we get the one-dimensional density distributions as shown in Fig. 5.

4. RESULTS

4.1. Wavelet analysis of 1D Zel’dovich density fields

From Fig. 3 we see that characteristics of the 1D density growth in our case is similar to the three-dimensional sim-

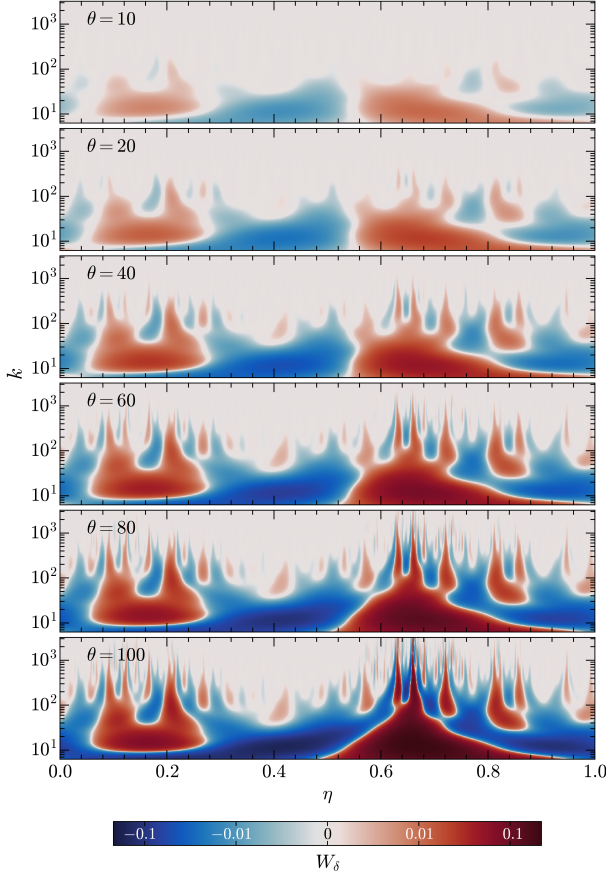


Figure 6. Wavelet transform plots for Zel'dovich density fields at epochs $\theta = 10, 20, 40, 60, 80$ and 100 . The vertical coordinate k represents $\sqrt{5}/2$ times the scale parameter w according to equation (21). These plots show the scale growth and the spatial location where it occurs.

ulations. With evolution of this simple system from linear ($\delta \ll 1$) to highly non-linear regime ($\delta \gg 1$) due to gravitational effects, structures become increasingly significant. For example, there is an obvious underdense region roughly ranging from $\eta \sim 0.3$ to $\eta \sim 0.5$, as well as a large overdense region which is next to it. Since these two distinct local environments in the universe are thought to have different effects on matter clustering (Abbas & Sheth 2005), we hope that wavelet methods are able to distinguish between them in our 1D toy model. In this section, we present the results for 1D matter clustering based on the CWT analysis.

4.1.1. Space-scale decomposition of the density fields

As stated by equation (3), the CWT is defined for the infinite input signal. Hence the finite signal must be padded with some values before the transform is performed. The usual padding schemes include zero padding, decay padding, periodic padding and symmetric padding (Addison 2017). In the present work, the density contrasts are periodically padded with themselves since they satisfy the periodic boundary con-

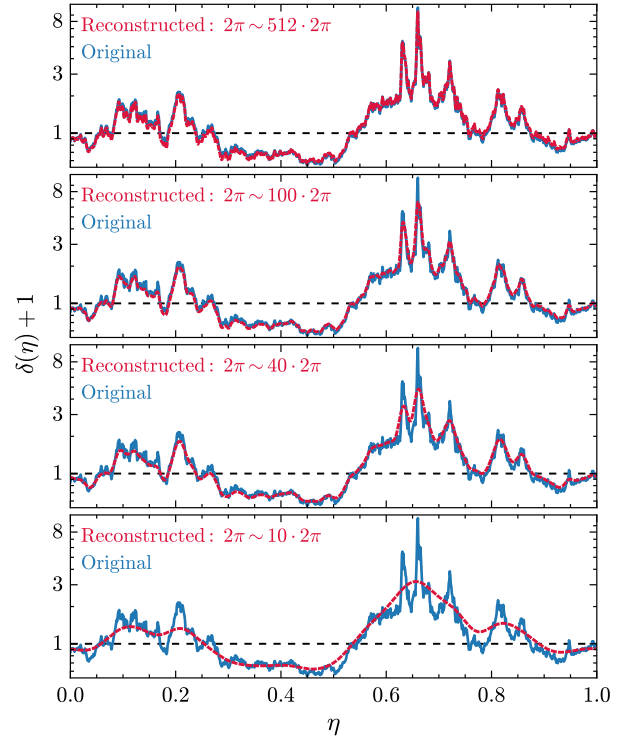


Figure 7. Wavelet reconstructions of Zel'dovich density field (red) at $\theta = 100$. The original density field (blue) is also shown here for comparison. With the upper scale limit decreases, the reconstructed density field becomes increasingly smooth.

dition. Then by employing the CWT, different features are picked out by GDW at each scale while retaining positional information, as illustrated in Fig. 6. From this figure, we can see that the wavelet coefficients $W_\delta(k, \eta)$ take values from negative (blue) to positive (red), reflecting that the density field is anti-correlated and correlated with GDW, respectively. The larger the absolute value of $W_\delta(k, \eta)$ (the darker the color), the stronger the (anti-)correlation.

Let's focus on $|W_\delta(k, \eta)|$. The characteristics of matter clustering will be seen qualitatively from the space-scale plane. From $\theta = 10$ to 20 , $|W_\delta(k, \eta)|$ evolves little with time and is dominated by large scale components with a relatively random spatial distribution. This indicates that the density field is almost homogeneous. At $\theta = 40$, the small-scale components start to become apparent owing to the gravitational interactions. Since then, $|W_\delta(k, \eta)|$ progressively increases with time. As a consequence, strongly structured patterns are formed in the space-scale plane at $\theta = 100$, suggesting that the density field is highly nonhomogeneous at this time. It is noteworthy that all scale components grow very significantly in the region from $\eta \sim 0.5$ to $\eta \sim 0.8$. As a contrast, there is almost no small scale components generated between $\eta \sim 0.3$ to $\eta \sim 0.5$, while there is a moderate increase at small scales in other regions. Based on these

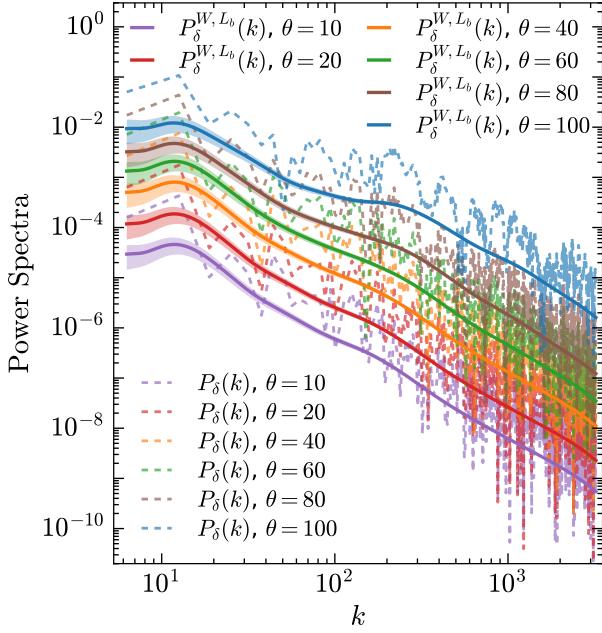


Figure 8. WPS (solid lines) and Fourier power spectra (dashed lines) of Zel'dovich density fields at epochs $\theta = 10, 20, 40, 60, 80$ and 100 , as labeled. The color bands corresponding to each WPS show their statistical errors estimated by equation (17).

simple analyses, we find that the CWT of density contrast reproduces its local evolutionary features very well.

Before further analysis with these space-scale components, we need to check whether the inverse transformation from them to the original density contrast can be achieved by equation (6). To this end, equation (6) is discretized into the following form

$$\delta^R(\eta) = \langle \delta \rangle + \sqrt{\frac{2}{\sqrt{5}}} \sum_k W_\delta(k, \eta) \frac{\Delta k}{\sqrt{k}}, \quad (25)$$

in which $\delta^R(\eta)$ is the reconstructed density field, and $\langle \delta \rangle$ is the overall averaged density contrast. k represents $\sqrt{5}/2$ times the scale parameter w , and there are 512 k evenly spaced as $k_n = 2\pi n$ with $n = 1, 2, \dots, 512$, and hence $\Delta k = 2\pi$. As a demonstration, we reconstruct the density field at $\theta = 100$ using equation (25). The reconstructed density field is shown by the red line in the top panel of Fig. 7, which fits well with the original density field. This fact implies that the wavelet space and the real space are equivalent to each other, and hence we can use $W_\delta(k, \eta)$ for further studies. In addition, if equation (25) is summed over a sub-range of the scale, then we can separate our interested components from the original density field. For example, as the upper limit of the summation is continuously reduced, small scale features are smeared out and the reconstructed density field becomes increasingly smoother, as illustrated in Fig. 7.

4.1.2. Wavelet power spectrum measurements

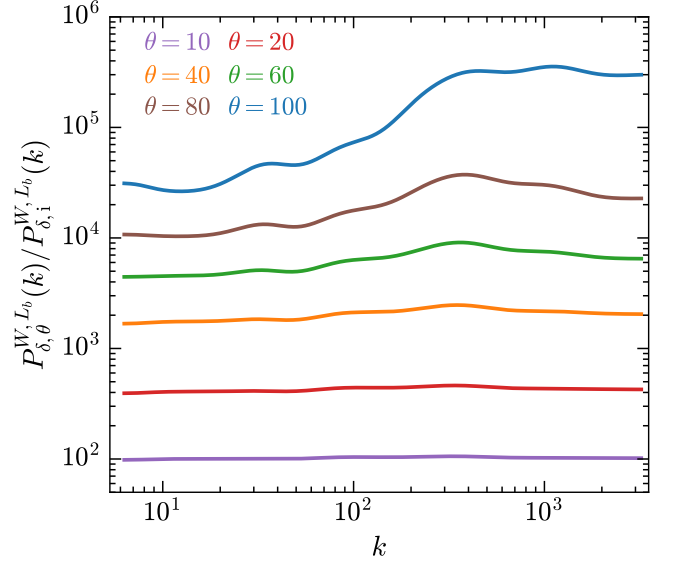


Figure 9. The ratio of the WPS at each epoch to the initial WPS. We observe that, $P_{\delta, \theta}^{W, L_b}(k) / P_{\delta, i}^{W, L_b}(k) \approx \theta^2$ at linear stages, while this relation does not hold at late times.

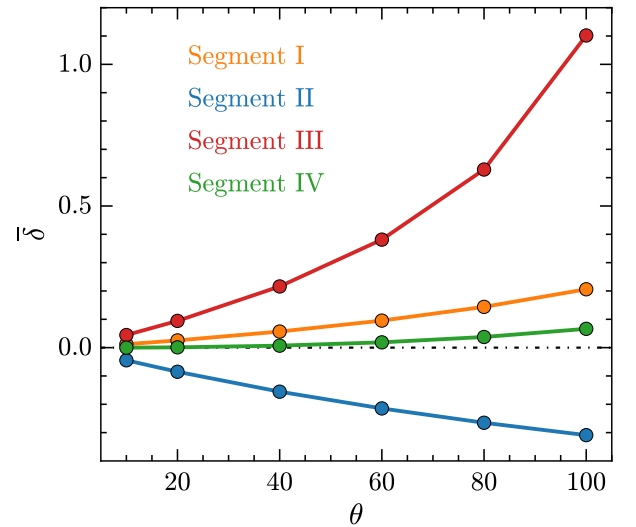


Figure 10. Time evolution of mean density contrasts within four local regions. Segment III evolves into a highly overdense region, while Segment II evolves into a underdense region. Segements I and IV are slightly overdense regions.

By averaging squared wavelet coefficients over a local spatial region, we thus obtain the local WPS. For a better understanding of the WPS, we first compare the global wavelet and Fourier power spectrum of 1D Zel'dovich fields. A main visible feature in Fig. 8 is that the WPS's are smoother than their Fourier counterparts, as expected by equation (10). These two types of power spectra have approximately same trends with comparable amplitudes. In fact, the global WPS is able to reproduce the correct exponent of the power-law

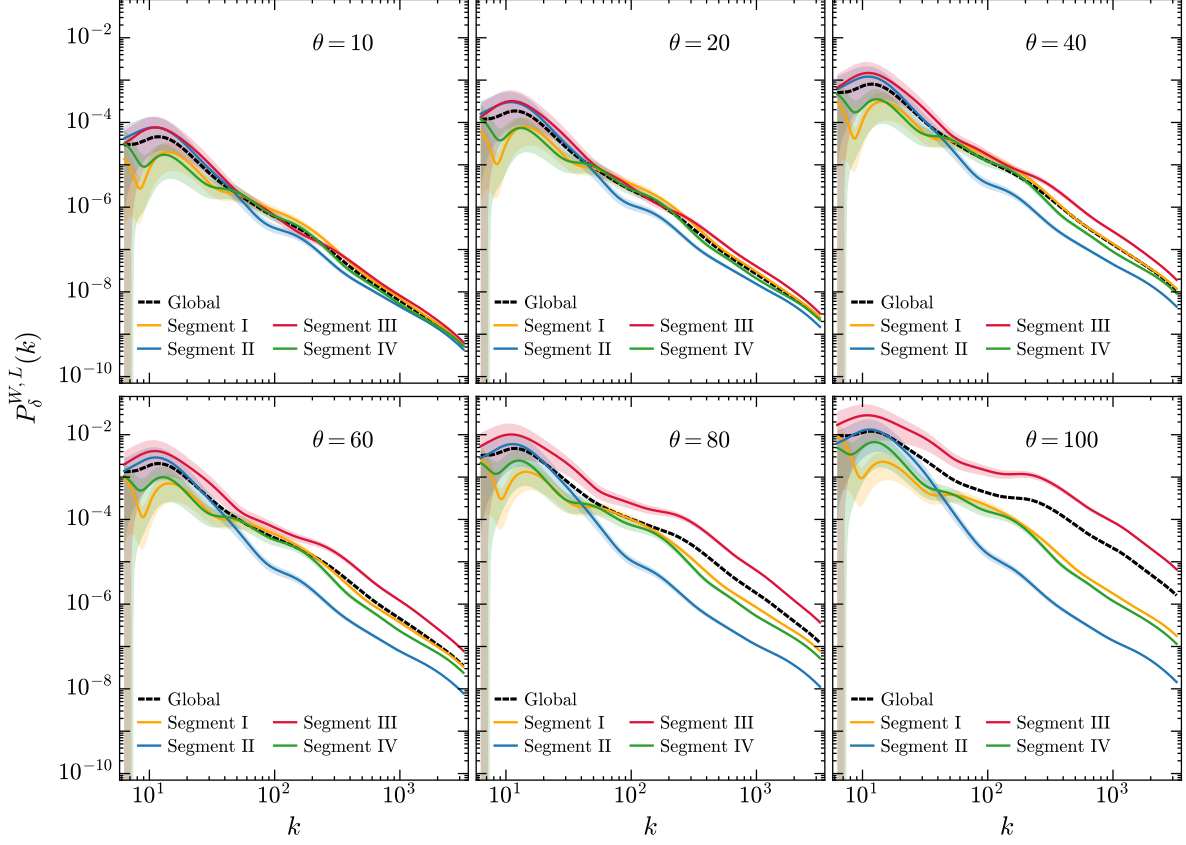


Figure 11. Local WPS for different density environments at times $\theta = 10, 20, 40, 60, 80$ and 100 . The shaded area for each curve represents the statistical error, from which we can see that those local WPS are less significant statistically on scales of $k \lesssim 40$.

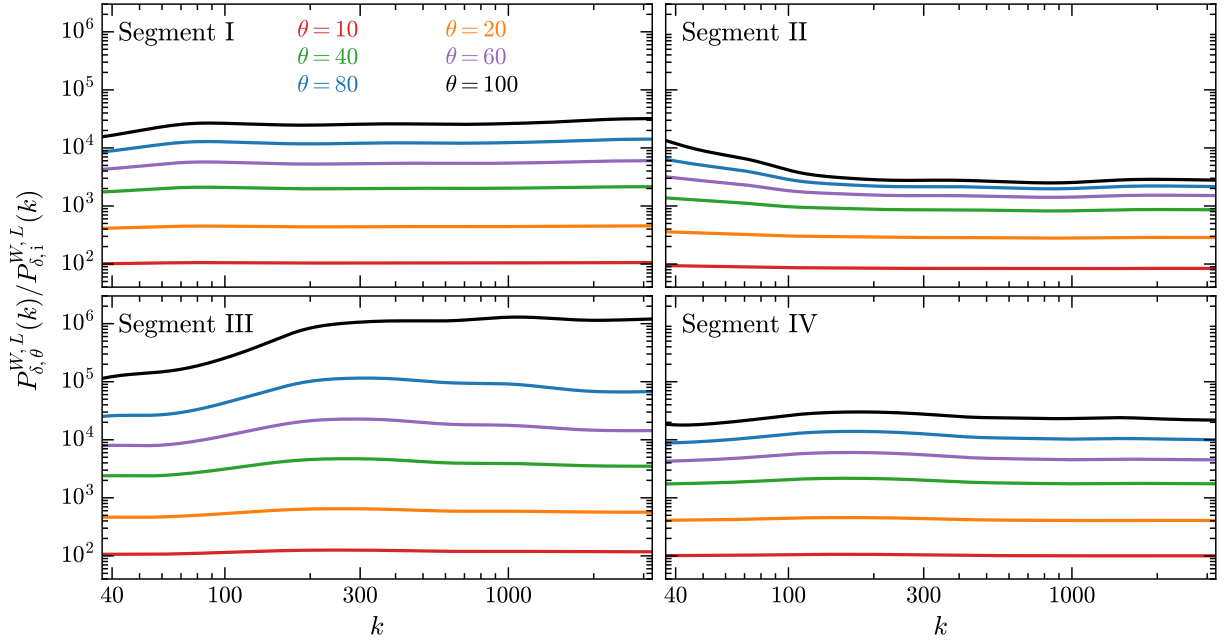


Figure 12. Local WPS for different density environments at times $\theta = 10, 20, 40, 60, 80$ and 100 relative to the initial WPS.

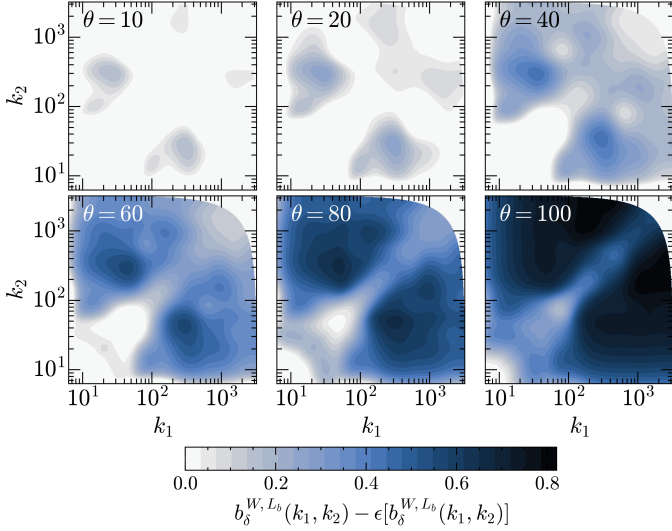


Figure 13. Contour plots of the WBCs with statistical noise level subtracted for density fields at times $\theta = 10, 20, 40, 60, 80$ and 100 . In these plots, values of the WBCs less than the statistical noise level are set to be zero.

Fourier power spectrum (Wang & He 2021), although it is not obvious for our 1D noisy data. From the WPS in Fig. 8, we see that the strength of clustering on small scales increases with time. Furthermore, by measuring the change of the WPS at each time relative to the initial WPS, it should help better demonstrate the nonlinear evolution of clustering. Since $\delta(\eta, t)$ approximately equals to $\theta(t)F(\eta)$ in the linear regime, there is a relation between the WPS of $\delta(\eta, t)$ and the initial one given by

$$P_{\delta,\theta}^{W,L_b}(k) \approx \theta^2 P_{\delta,i}^{W,L_b}(k). \quad (26)$$

Hence if the ratio of these two WPS, $P_{\delta,\theta}^{W,L_b}(k)/P_{\delta,i}^{W,L_b}(k)$, is not scale dependent, then the growth of the density fluctuations is linear. We show this ratio for times $\theta = 10, 20, 40, 60, 80$ and 100 in Fig. 9. Obviously, $P_{\delta,\theta}^{W,L_b}(k)/P_{\delta,i}^{W,L_b}(k)$ is almost constant over the entire scale range at $\theta = 10$ and 20 , suggesting that the density contrast is linear. However, this ratio becomes scale dependent at the time $\theta = 40$ and there is a mild bump around $k \approx 300$, which means that there are a few newly generated scale components and the density contrast is quasi-nonlinear. Since then, this bump has been enhanced by nonlinear effects with time to $\theta = 80$, while the ratio remains approximately flat on large scales of $k \lesssim 20$. At the time $\theta = 100$, the ratio increases more significantly on small scales thus leading to a plateau at scales of $k \gtrsim 300$, implying that the density field has developed into the highly non-linear regime.

Next, we turn our attention to the environmental dependence of matter clustering. To do this, we split the density field into four consecutive segments labeled I, II, III and IV. The spatial extent spanned by each segment and the mean

density within that local space at each time are listed in Table 2. The evolutionary trends of these four local mean densities are more clearly depicted in Fig. 10. We see that Segment III represents the highly overdense environment, and both Segments I and IV represent the slightly overdense environment, while Segment II represents the underdense environment. These different density environments are expected to exhibit distinct clustering characteristics from each other. Therefore, it is instructive to examine the local WPS for each environment, as shown in Fig. 11. Each subplot shows the WPS for different regions at the same time. At linear stages ($\theta = 10$ and 20), all of these local power spectra roughly converge to the global WPS. Starting from $\theta = 40$, however, the divergence between these local power spectra becomes more and more significant with time. For the highly overdense environment, i.e. Segment III, its WPS is more enhanced than all other regions over the entire scale range. In contrast, the WPS for the underdense environment (Segment II) is more suppressed than all other regions on scales of $k \gtrsim 40$. For Segments I and IV, as slightly overdense regions, the amplitudes of their WPS are very close to each other and fall between II and III on the scales of $k \gtrsim 40$. Notice that as the scale becomes larger, the statistical error in the power spectrum becomes increasingly large to the extent that it does not give a significant description of matter clustering in the range $k \lesssim 40$, due to the wavelet coefficients being non-orthogonal and the length of local region being too short. Even so, the WPS is still able to give a meaningful interpretation over a relatively large scale range.

In Fig. 12, we also measure the local WPS at each time relative to its corresponding initial WPS within the scale range $k \gtrsim 40$ where statistical errors are smaller. For all segments, we see that $P_{\delta,\theta}^{W,L}(k)/P_{\delta,i}^{W,L}(k)$ approximates to θ^2 at stages of $\theta = 10$ and 20 . However, at late stages, the evolutionary trends of Segments II and III are completely opposite. For Segment II, the growth of small-scale components is getting slower, but for Segment III, the small-scale components are growing faster and faster. Although the WPS's of Segments I and IV are very similar, there are visible differences between them. Specifically, the former has a slightly upward tilt on small scales, while the latter remains roughly horizontal.

Based on these facts, we find that WPS is fully capable of detecting the effects of density environments on matter clustering. However, as pointed out above, the density field evolves into the non-linear regime at late times, indicating that there are couplings between different scale components. The WPS, as two-point statistics, cannot determine such scale-coupling since it does not contain phase information. To detect scale-coupling, we measure the WBC, which is the lowest order statistics sensitive to nonlinear couplings between different scales of matter density field.

Table 2. We split the density field at each time into four consecutive segments. The spatial range spanned by each segment and the corresponding local mean density contrast at times of $\theta = 10, 20, 40, 60, 80$ and 100 are listed.

Segment	Spatial Range	The mean density contrast $\bar{\delta}$					
		$\theta=10$	20	40	60	80	100
I	$0.00 \lesssim \eta \lesssim 0.27$	0.012	0.025	0.056	0.095	0.144	0.206
II	$0.27 \lesssim \eta \lesssim 0.54$	-0.045	-0.085	-0.155	-0.214	-0.265	-0.309
III	$0.54 \lesssim \eta \lesssim 0.78$	0.044	0.094	0.216	0.381	0.629	1.102
IV	$0.78 \lesssim \eta \lesssim 1.00$	0.000	0.001	0.007	0.018	0.037	0.066

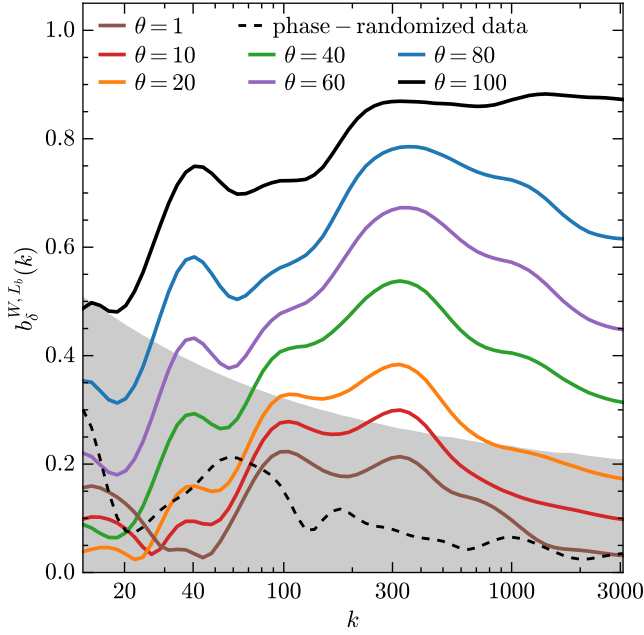


Figure 14. Summed WBC for density fields at times $\theta = 1, 10, 20, 40, 60, 80$ and 100 (solid lines). The summed WBC for the phase-randomized data obtained from the density field at $\theta = 100$ is indicated by the black dashed line and that of initial density field ($\theta = 1$) is indicated by the brown solid line as a comparison. The gray area represents the region where the summed WBC is less than the statistical noise level.

4.1.3. Wavelet bicoherence measurements

Fig. 13 shows the time evolution of matter WBC with statistical noise subtracted, i.e. $b_\delta^{W, L_b}(k_1, k_2) - \epsilon[b_\delta^{W, L_b}(k_1, k_2)]$. Note that $b_\delta^{W, L_b}(k_1, k_2)$ is symmetric about the diagonal where $k_1 = k_2$, as indicated by equations (13) and (14). So we will only concern the part below (or above) this diagonal. For visual convenience, values of bicoherence less than the noise level are not considered, because they are less significant physically. To better understand the statistical noise level, as suggested by van Milligen et al. (1995a,b), we perform the FFT on the highly non-linear density field at time $\theta = 100$, and give each Fourier component a ran-

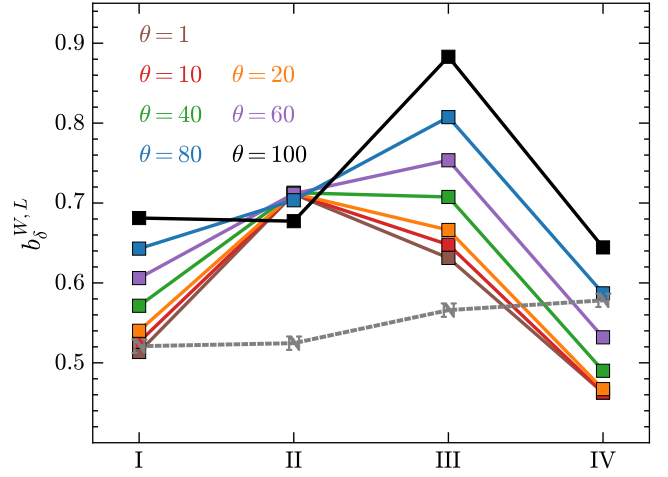


Figure 15. Time evolution of the total WBC from the initial time $\theta = 1$ to $\theta = 100$ in Segments I, II, III and IV. The marker ‘N’ indicates the noise level for each segment.

dom phase while maintaining its amplitude, then we perform the inverse FFT to get a new set of data. Such new phase-randomized density field is expected to have no structures induced by scale-coupling, while its power spectrum is identical to that of the raw density field, in which structures are well formed, as is illustrated in Fig. 14. It can be seen that the summed WBC of the density field at $\theta = 100$ is much higher than that of the phase-randomized version, which falls below the noise level along with the initial density field. Thus the statistical noise level provides us a criterion to discriminate matter distributions with structures formed from those without. Accordingly, looking at Fig. 13 and 14 together, there is a very weak coupling between large scales around $k \sim 10$ and intermediate scales around $k \sim 300$ at times $\theta = 10$ and 20 . Gradually, the scale-coupling becomes more and more significant with time and eventually spreads to the whole scale range, which implies that the matter distribution becomes more and more structured.

In Fig. 15, we consider the evolution of the total WBC with time in the consecutive segments I, II, III and IV. An

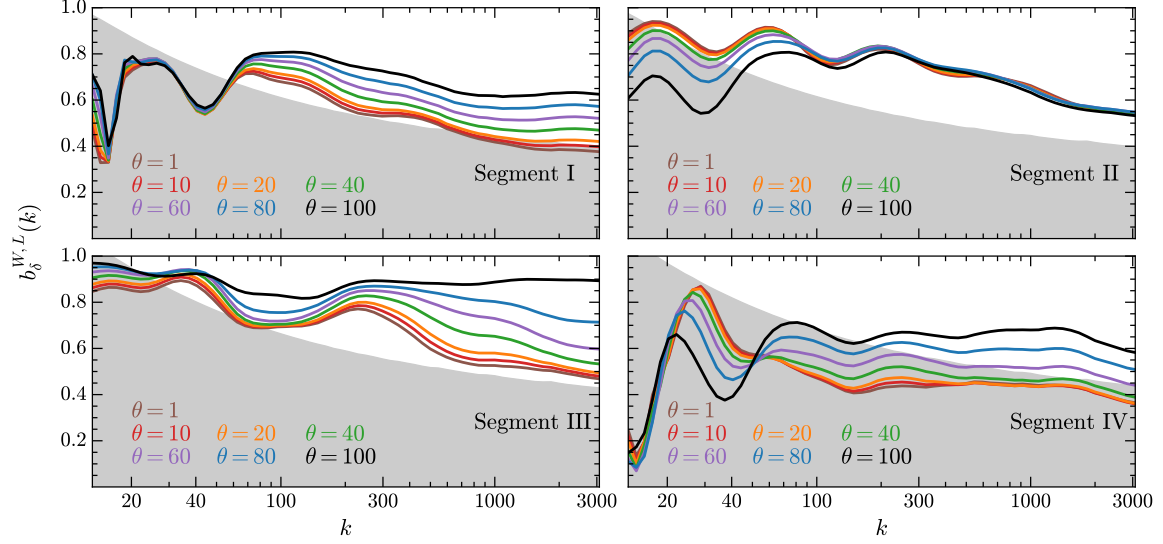


Figure 16. The summed WBC of four consecutive segments marked I, II, III and IV at times $\theta = 1, 10, 20, 40, 60, 80$ and 100 . The grey region of each subplot indicates where the summed WBC are below the statistical noise level.

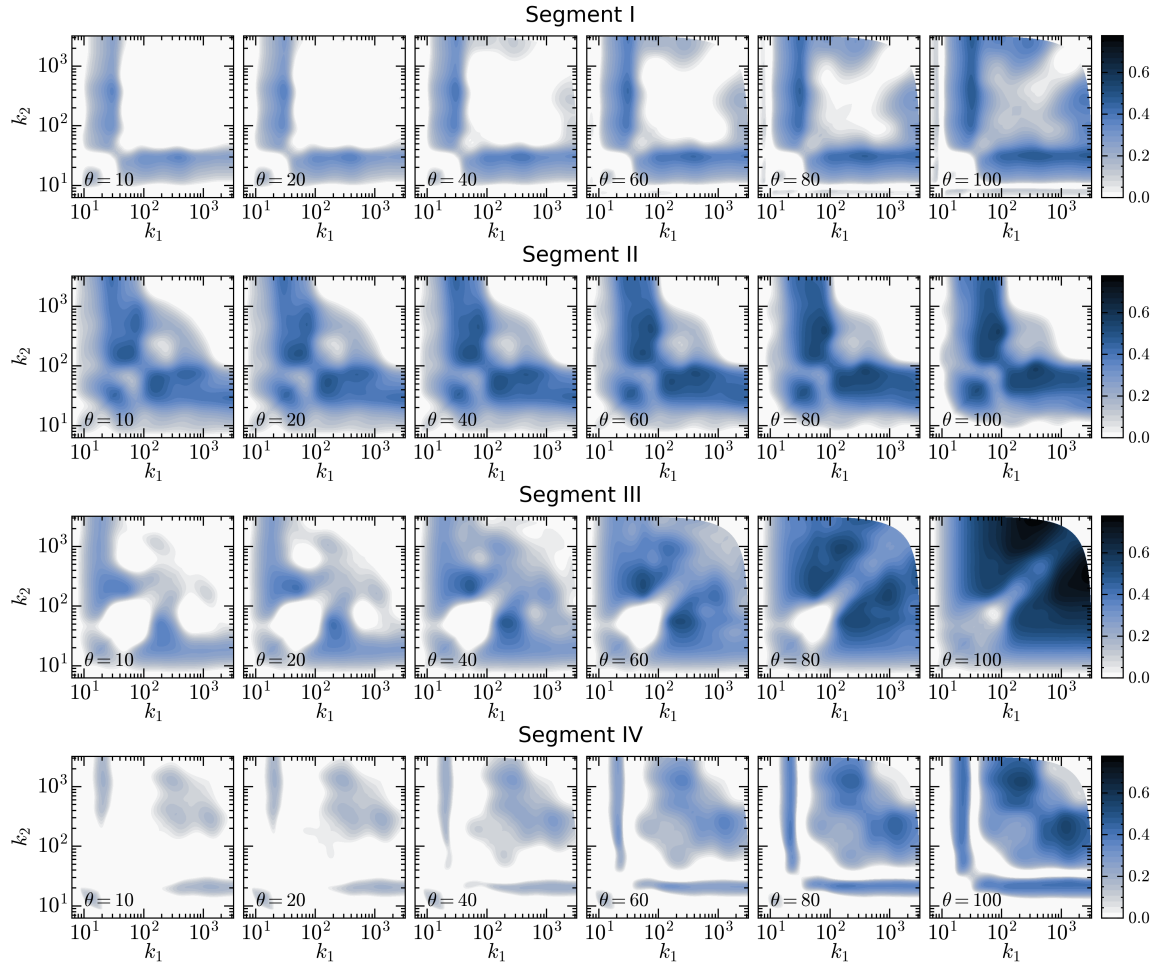


Figure 17. WBC with statistical noise subtracted, i.e. $b_{\delta}^{W,L}(k_1, k_2) - \epsilon[b_{\delta}^{W,L}(k_1, k_2)]$ for local segments at times $\theta = 10, 20, 40, 60, 80$ and 100 . For easier visual description, values of the WBC less than the statistical noise level are set to be zero in each subplot.

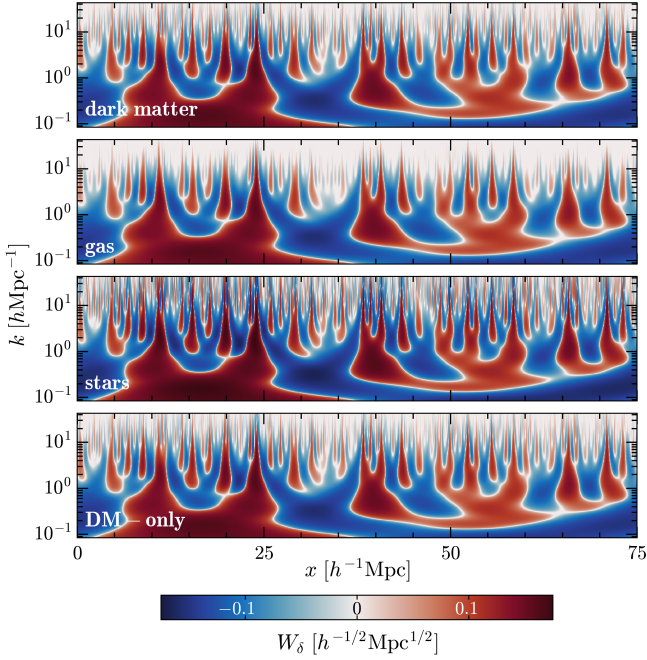


Figure 18. Wavelet transform plots of the 1D projected density fields for the dark matter, gas, stars and the DM-only simulation at redshift $z = 0$.

interesting phenomenon is that the degree of non-linearity in Segment II, the underdense region, is much higher than noise level at the initial time, and this non-linearity is less evolved. On the other hand, the non-linearity is more evolved in overdense regions, although it is very weak at the initial time. In particular, Segment III, as a highly overdense region, has the strongest non-linearity at late times. This implies that structure formation occurs mainly in Segment III. Furthermore, we examine the scale-coupling for these segments by measuring their WBC and summed WBC at different times and corresponding results are shown in Figs. 16 and 17. Consistent with the results in Fig. 15, the estimated WBC and summed WBC in Segment II exhibit significant values between widely separated scales at the initial time, because the matter distribution within such a underdense region is left-skewed. Both WBC and summed WBC in Segment II barely evolve with time, indicating that there is almost no structure formation in this region. Also, Segment III shows a notable coupling between scale bands $20 \lesssim k \lesssim 100$ and $100 \lesssim k \lesssim 500$ at initial stages, due to the matter distribution in such a highly overdense region being right-skewed. Unlike Segment II, the WBC and summed WBC of Segment III evolves the most dramatically, which indicates that the matter becomes increasingly clustered. For Segments I and IV, the bicoherences are below or close to the statistical noise level at initial stages and evolve mildly with time, which means that the matter experiences moderate structure formation in these two slightly overdense regions.

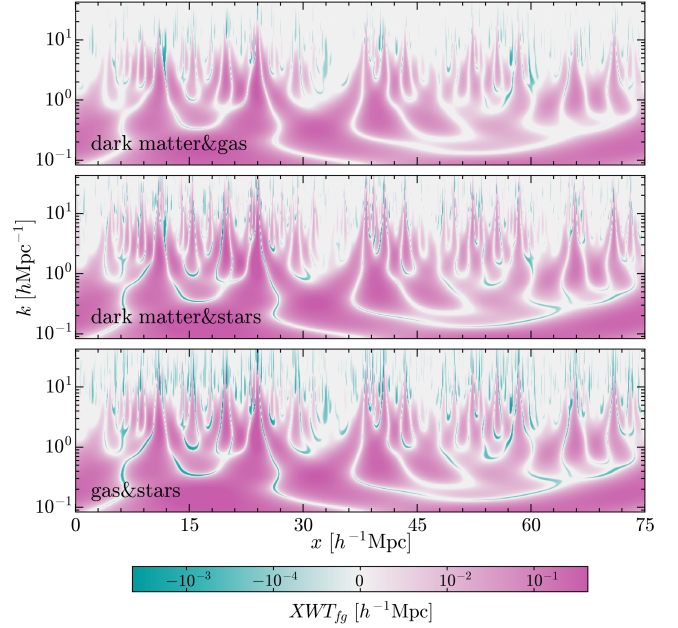


Figure 19. Cross-wavelet transforms between dark matter, gas and stellar density fields at redshift $z = 0$.

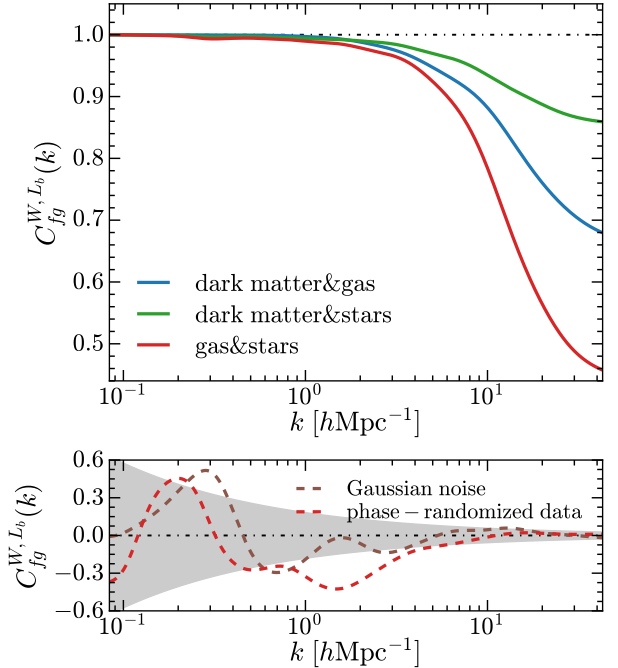


Figure 20. WCC functions. The top panel: WCCs between different density fields, where f and g stand for dark matter, gas or stars, respectively. The bottom panel: the brown dashed line represents the WCC between two Gaussian noise processes. The red dashed line represents the WCC between phase-randomized density fields of dark matter and gas.

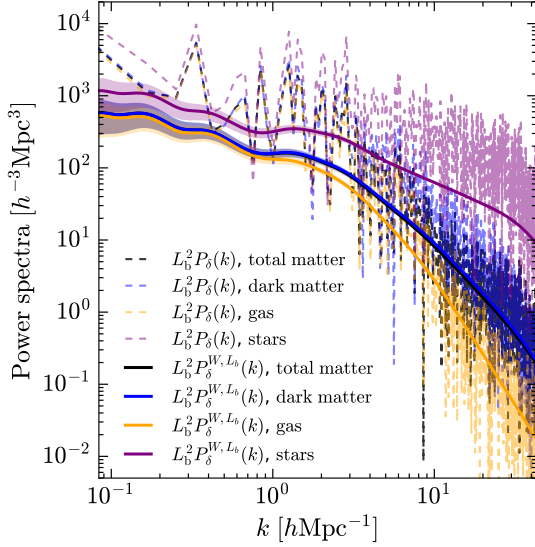


Figure 21. The 1D wavelet and Fourier power spectra, scaled by the square of the box size $L_b = 75 h^{-1}\text{Mpc}$, for different matter components at redshift $z = 0$. The color band corresponding to each WPS indicates its statistical error estimated by equation (17).

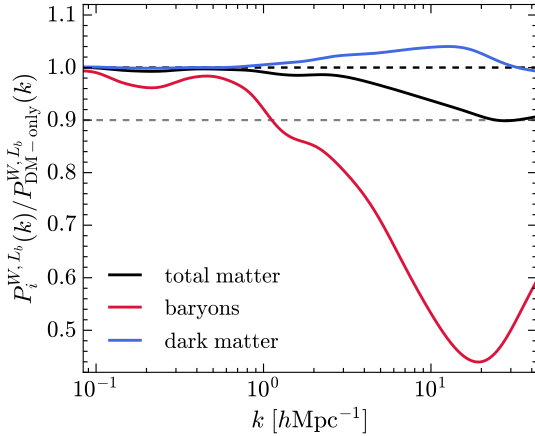


Figure 22. Impact of baryons on the WPS at redshift $z = 0$, measured by $P_i^{W,L_b}(k)/P_{\text{DM-only}}^{W,L_b}(k)$, where i denotes total matter, baryons and dark matter, respectively.

4.2. Wavelet analysis of the 1D projected density fields of the IllustrisTNG simulation

In this subsection, we will explore if wavelet-based statistical methods are able to characterize the baryonic effects on matter clustering in one-dimensional case. Therefore, we first decompose the 1D projected density fields of dark matter, gas, stars and corresponding DM-only simulation into different scale components at any spatial location, which are shown in Fig. 18. The wavelet transforms of different matter exhibit similar characteristics qualitatively. While there are more small-scale components in the wavelet transform of stars than that of dark matter, the gas shows a deficit of small

scale structures. More quantitative results for the WCC, WPS and WBC are given below.

Since Zel'dovich approximation is only involved in a single matter component, we cannot use it to discuss the importance of the WCC in analyzing matter clustering. To remedy this, we introduce density fields for different matter components of the TNG100 simulation and measure the WCCs between them. In Fig. 19, we plot the XWT between dark matter, gas and stars at $z = 0$. The XWT gives the deviation between two matter distributions in both space and scale simultaneously. Positive values of XWT imply in-phase and negative ones imply out-of-phase. So we see from Fig. 19 that the density distributions of dark matter, gas and stars are in-phase on most areas of space-scale plane. There are a few out-of-phase regions, which are mainly distributed on small scales. Therefore all these matter components generally trace each other well, especially on large scales. To make it more explicit, we consider the normalized cross-correlation functions C_{fg}^{W,L_b} between different matter components, as defined by equation (12), and the results are shown in Fig. 20. On large scales, all WCCs approach one, while on small scales, dark matter and stars are more correlated than other pairs, which may suggest the alignment of the distributions of stars with the dark matter cusps.

Fig. 21 compares the global WPS and Fourier power spectra for different matter distributions. As opposed to the 1D Fourier power spectra being spiky and noisy, the WPS's for 1D density distribution are much smoother and therefore easier to interpret. It can be seen that both amplitudes of these two types of spectra multiplied by the square of box size are roughly consistent with the three-dimensional Fourier matter power spectra in Springel et al. (2018). The WPS of the total matter falls slightly below that of the dark matter at small scales. The gas becomes significantly less clustered than dark matter at intermediate and small scales, while the stellar mass shows a very strong clustering. Furthermore, we examine the impact of baryons on the matter clustering by defining the ratio between the WPS of total matter in full physics simulation and that of the corresponding DM-only simulation, which is shown in Fig. 22. We see that the total matter WPS is reduced on scales $k \gtrsim 1 h\text{Mpc}^{-1}$ relative to the DM-only WPS, with a 10% suppression around $k \sim 20 h\text{Mpc}^{-1}$, which can be mainly credited to active galactic nucleus (AGN) feedback. Note that our ratio $P_{\text{total matter}}^{W,L_b}(k)/P_{\text{DM-only}}^{W,L_b}(k)$ is somewhat different from the ratio of Fourier power spectra for 3D matter distributions, which shows a maximum suppression of about 20% at around $10 h\text{Mpc}^{-1}$ (Springel et al. 2018). Such difference is probably due to the fact that we consider only the 1D projection of the density field slice in a particular direction.

The change in the total matter WPS in the full physics simulation comes from two aspects: (1) the redistribution of

baryons by non-gravitational physics, and (2) the change in the dark matter distribution resulted from the gravitational coupling of baryons and dark matter, which is called the back-reaction (van Daalen et al. 2020). To consider the former effect, we compare the WPS of total baryons to that of DM-only simulation, as shown in Fig. 22. We see that the WPS of baryons is increasingly suppressed as the scale decreases until the maximum suppression approximately of 55% is reached at $k \sim 20 h\text{Mpc}^{-1}$. This suppression is caused by the large amount of gas being ejected from the halo due to AGN feedback, whereas the upturn in the baryonic power spectrum at $k \gtrsim 20 h\text{Mpc}^{-1}$ is owing to star formation and gas cooling. To consider the back-reaction of baryons on dark matter, we measure the WPS of dark matter relative to that of the DM-only simulation, also shown in Fig. 22. The modification to the dark matter distribution alone is fairly large but weaker than the modification to baryons, suggesting that the great change in the baryon distribution relative to the dark matter distribution caused by galaxy formation is the determinant of the change in the WPS of total matter.

We also calculate the WBCs for these density fields to detect the coupling between different scale components, which we show in Fig. 23. The WBC for total matter exhibits similar behaviors to that of dark matter due to gravitational effects: scales of 0.2 to 0.4 $h\text{Mpc}^{-1}$ couple with those of 1 to 2 $h\text{Mpc}^{-1}$, and scales of 1 to 10 $h\text{Mpc}^{-1}$ couple with those of 10 to 40 $h\text{Mpc}^{-1}$. The former reflects the non-linear influence of the large scale environment on relatively small scales, while the latter may reflect the non-linear scale-coupling within halo scales. In fact, baryon physical processes lead to certain differences between the WBCs of total matter and dark matter. As shown in Fig. 24, the summed WBC for total matter starts to differ from that of the DM-only simulation at the scale $k = k_1 + k_2 \sim 2 h\text{Mpc}^{-1}$. Moreover, the summed WBC of baryons is enhanced to a greater extent than the summed WBC of dark matter compared to that of DM-only simulation on scales $k = k_1 + k_2 \gtrsim 2 h\text{Mpc}^{-1}$. There are two reasons of the enhancement of WBC for baryons. The first, from Figs. 23 and 24, we see that the enhancement on large scales is due to the nonlinear correlation between larger-than-halo scales and smaller scales of gas, probably as a result of feedback processes. The second, the enhancement on small scales is due to the coupling with small scales of stars resulted from star formation within dark halos.

5. DISCUSSION AND CONCLUSIONS

The clustering of matter is an intricate process. In addition to redshift and scale dependence, the density environment plays a very important role on the clustering. When the usual Fourier statistics are utilized to examine the scale dependence, we are unable to take into account the effect of

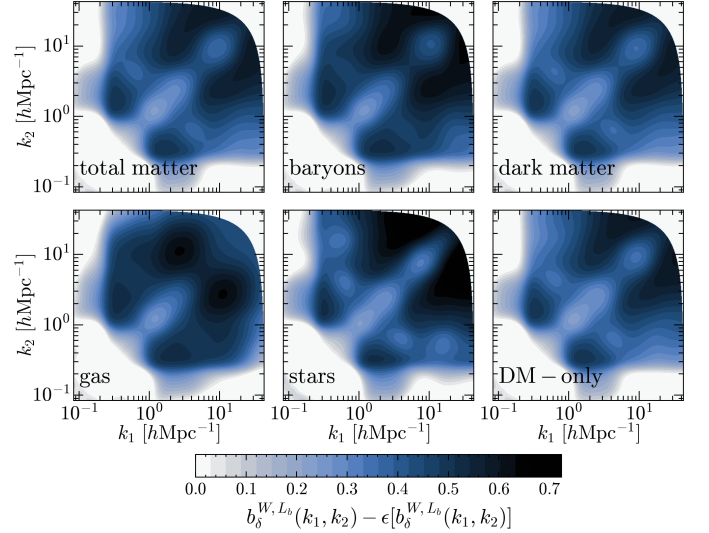


Figure 23. WBCs with noise level subtracted for different matter components at redshift $z = 0$. In these plots, values of the WBC less than the statistical noise level are set to be zero. In both this figure and the next, ‘baryons’ refers to ‘gas’ + ‘stars’.

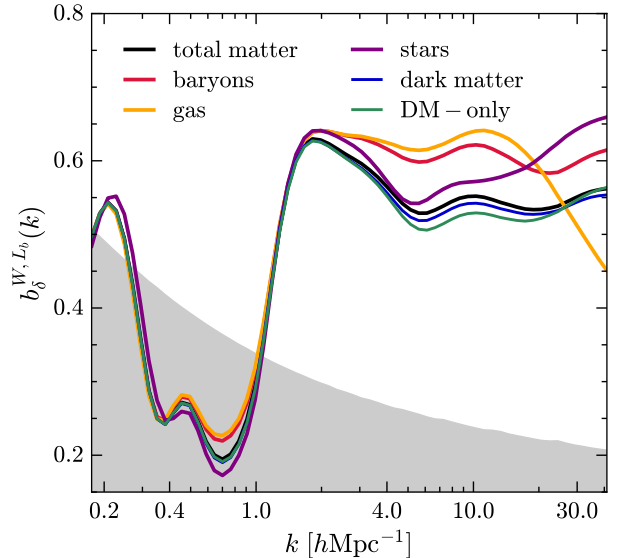


Figure 24. Summed WBCs for different matter components at redshift $z = 0$. They are much higher than the noise level on scales $k = k_1 + k_2 \gtrsim 2 h\text{Mpc}^{-1}$, while they are less significant on scales $k = k_1 + k_2 \lesssim 1 h\text{Mpc}^{-1}$.

environment, since the local density information contained in the physical space is smeared out. Therefore, we need better tools to consider both scale and environment dependence simultaneously, and the continuous wavelet transform is such a tool of good performance.

In this work, we introduce some statistical quantities formulated on the specific wavelet function – Gaussian-derived wavelet, which is a real valued continuous wavelet designed

by taking the first derivative of the Gaussian smoothing function with respect to the scale parameter. With such a wavelet construction scheme, the original signal can be recovered from wavelet coefficients easily. These wavelet statistics we used include the wavelet power spectrum, the wavelet cross-correlation and the wavelet bicoherence. To better describe the results, we also present the methods for estimating the statistical error, and discuss the relationship between the scale parameter and the Fourier wavenumber.

To reveal the usefulness of wavelet statistics in analyzing matter clustering, we use two sets of one-dimensional cosmic density fields throughout the work. Firstly, the time evolution of the density distributions obtained from the Zel'dovich approximation is analyzed by measuring their wavelet power spectra and bicoherences. Measurements show that the global wavelet power spectrum on small scales increases more significantly with time than that on large scales, which is generally in agreement with the Fourier case.

For manifesting the capability of wavelet statistics to perform local spectral analysis, we divide the 1D Zel'dovich density field at each time into four consecutive segments. All the local wavelet power spectra for these segments almost converge to the global wavelet power spectrum at linear stages. However, the difference between the local power spectra and the global wavelet power spectrum becomes progressively larger with time due to nonlinear effects. In particular, the wavelet power spectrum of Segment III (highly overdense environment) is significantly greater than those of other segments on scales $k \gtrsim 40$, where statistical errors are smaller, which implies that structures on these scales are generated in this region at nonlinear stages. Another striking feature is that the growth of the wavelet power spectrum in Segment II (underdense environment) is severely suppressed on scales $k \gtrsim 40$, meaning that there are very few structures on these scales generated in this region at later times. Moreover, measurements of the wavelet bicoherences show that the scale coupling occurs mainly in the Segment III, whereas there is almost no scale coupling in Segment II at late epochs. Both the wavelet power spectrum and the wavelet bicoherence in Segment I and IV exhibit similar behaviors to and fall between those in Segment II and III, probably because Segment I and IV are slightly overdense environments. These results illustrate that wavelet statistics can simultaneously take

into account the effects of both environment and scale on matter clustering.

As supplementary, we apply the wavelet cross-correlation, the wavelet power spectrum, and the wavelet bicoherence to the 1D projected density fields of IllustrisTNG simulation at $z = 0$ to detect baryonic effects. Measurements of the wavelet cross-correlations between different matter components suggest that they trace each other well on large scales, while the biases between them are more pronounced on smaller scales. Measurements of the wavelet power spectra show that clustering of total matter is suppressed on scales $k \gtrsim 1 h\text{Mpc}^{-1}$. Hence our results of 1D density fields are in consistent qualitatively with three-dimensional Fourier-based results in [Springel et al. \(2018\)](#). Additionally, the wavelet bicoherence of total matter is enhanced relative to that of DM-only simulation, which implies that baryon physical processes lead to a stronger nonlinear scale coupling. These facts demonstrate that wavelet statistics can give rather meaningful results, even though our density data are one-dimensional with only 1024 data points.

According to the discussions above, we believe that statistics with the continuous wavelet transform are very useful for studying the matter clustering, especially its dependence on both the scale and the environment. In future works, we will explore more applications of this powerful analysis method in the studies of large-scale structures of the Universe.

ACKNOWLEDGMENTS

YW especially thanks Dr. van Milligen for helpful discussions on the statistical error estimation for wavelet statistical quantities. PH acknowledges the support by the Natural Science Foundation of Jilin Province, China (No. 20180101228JC), and by the National Science Foundation of China (No. 11947415, 12047569). In this work, we used the data from IllustrisTNG simulations. The IllustrisTNG simulations were undertaken with compute time awarded by the Gauss Centre for Supercomputing (GCS) under GCS Large-Scale Projects GCS-ILLU and GCS-DWAR on the GCS share of the supercomputer Hazel Hen at the High Performance Computing Center Stuttgart (HLRS), as well as on the machines of the Max Planck Computing and Data Facility (MPCDF) in Garching, Germany.

REFERENCES

- Abbas, U., & Sheth, R. K. 2005, *MNRAS*, 364, 1327
- Abdulazeez, A. M., Zeebaree, D. Q., Zebari, D. A. et al. 2020, *JSCDM*, 1, 31
- Addison, P. S. 2017, *The Illustrated Wavelet Transform Handbook: Introductory Theory and Applications in Science Engineering, Medicine and Finance*, (2nd ed.; CRC press)
- Addison, P. S. 2018, *Phil. Trans. R. Soc. A*, 376, 20170258
- Aguiar-Conraria, L., & Soares, M. J. 2014, *J. Econ. Surv.*, 28, 344
- Arnalte-Mur, P., Labatie, A., Clerc, N., et al. 2012, *A&A*, 542, A34
- Chisari, N. E., Mead, A. J., Joudaki, S., et al. 2019, *Open J. Astrophys.*, 2, 4

- Chui, C. K. 1997, *Wavelets: a mathematical tool for signal analysis*, (SIAM)
- Delprat, N., Escudé, B., Guillemain, P., et al. 1992, *IEEE Trans. Inf. Theory*, 38, 644
- Fang, L.-Z., & Feng, L.-L. 2000, *ApJ*, 539, 5
- Flin, P., & Krywult, J. 2006, *A&A*, 450, 9
- Frick, P., Beck, R., Berkhuijsen, E. M., et al. 2001, *MNRAS*, 327, 1145
- Fujiwara, Y., & Soda, J. 1996, *Prog. Theor. Phys.*, 95, 1059
- Gouda, N., & Nakamura, T. 1989, *Prog. Theor. Phys.*, 81, 633
- Gu, J.-H., Xu, H.-G., Wang J.-Y., et al. 2013, *ApJ*, 773, 38
- He, P., Liu, J., Feng, L.-L. 2006, *PhRvL*, 96, 051302
- Hudgins, L., Friehe, C. A., & Mayer, M. E. 1993, *PhRvL*, 71, 3279
- Khalifa, O. O., Harding, S. H., & Hashim, A. H. A. 2008, *SPIJ*, 2, 17
- Labatie, A., Starck, J. L., & Lachièze-Rey, M. 2012, *ApJ*, 746, 172
- Liu, J.-R., & Fang, L.-Z. 2008, *ApJ*, 672, 11
- Mallat, S. 2008, *A Wavelet Tour of Signal Processing: The Sparse Way*, (3rd ed.; Academic Press)
- Man, Z.-Y., Peng, Y.-J., Kong, X. et al. 2019, *MNRAS*, 488, 89
- Manfredi, G., Rouet, J. L., Miller, B., et al. 2016, *PhRvE*, 93, 042211
- Marinacci, F., Vogelsberger, M., Pakmor, R., et al. 2018, *MNRAS*, 480, 5113
- Martínez, V. J., Paredes, S., & Saar, E. 1993, *MNRAS*, 260, 365
- Meyers, S. D., Kelly, B. G., & O'Brien, J. J. 1993, *Mon. Wea. Rev.*, 121, 2858
- Miller, B. N., & Rouet, J. L. 2010, *J. Stat. Mech. Theory Exp.*, P12028.
- Naiman, J. P., Pillepich, A., Springel, V., et al. 2018, *MNRAS*, 477, 1206
- Nelson, D., Pillepich, A., Springel, V., et al. 2018, *MNRAS*, 475, 624
- Pando, J., & Fang, L.-Z. 1996, *ApJ*, 459, 1
- Pando, J., Lipa, P., Greiner, M. et al. 1998, *ApJ*, 496, 9
- Peng, Y.-J. et al. 2010, *ApJ*, 721, 193
- Pillepich, A., Nelson, D., Hernquist, L., et al. 2018, *MNRAS*, 475, 678
- Rozgacheva, I. K., Boriso, A. A., Agapov, A. A., et al. 2012, preprint (arXiv:1201.5554)
- Schwinn, J., Baugh, C. M., Jauzac, M., et al. 2018, *MNRAS*, 481, 4300
- Shandarin, S. F., & Zel'dovich, Y. B. 1989, *RMP*, 61, 185.
- Shi, X., Nagai, D., & Lau, E. T. 2018, *MNRAS*, 481, 1075
- Soda, J., & Suto, Y. 1992, *ApJ*, 396, 379
- Springel, V. 2010, *MNRAS*, 401, 791
- Springel, V., Pakmor, R., Pillepich, A., et al. 2018, *MNRAS*, 475, 676
- Tabatabaei, F. S., Berkhuijsen, E. M., Frick, P., et al. 2013, *A&A*, 557, A129
- Tatekawa, T., & Maeda, K. I. 2001, *ApJ*, 547, 531
- Tegmark M. et al. 2004, *ApJ*, 606, 702
- Tian, H.-J., Neyrinck, M. C., Budavári, T., et al. 2011, *ApJ*, 728, 34
- Torrence, C., & Compo, G. P. 1998, *Bull. Am. Meteorol. Soc.*, 79, 61
- van Daalen, M. P., McCarthy, I. G., Schaye, J. 2020, *MNRAS*, 491, 2424
- van Milligen, B. P., Hidalgo, C., & Sánchez, E. 1995, *PhRvL*, 74, 395
- van Milligen, B. P., Sánchez, E., Estrada, T., et al. 1995, *Phys. Plasmas*, 2, 3017
- van Milligen, B. P., Hidalgo, C., Sánchez, E., et al. 1997, *Rev. Sci. Instrum.*, 68, 967
- Wang, Y. et al. 2018, *ApJ*, 868, 130
- Wang, Y., & He P. 2021, *Commun. Theor. Phys.*, 73, 095402
- Yang, H.-Y., He, P., Zhu, W.-S. et al. 2020, *MNRAS*, 498, 4411
- Zel'dovich, Y. B. 1970, *A&A*, 5, 84